Research Article

Intervalence charge transfer and thermodynamic effects on the photocatalytic performance of Fe/Mo single and codoped TiO$_2$ thin films

Divyank Mittal[1,2] · Wen-Fan Chen[1] · Pramod Koshy[1] · Hsin-Kai Chen[1] · Imrana Kabir[1] · Yue Jiang[1] · Zhiyuan Liu[1] · Charles Christopher Sorrell[1]

Abstract

Fe/Mo single doped and codoped TiO$_2$ thin films were spin coated on polished fused silica substrates and annealed in air at 450 °C for 2 h. The XPS data for the anatase thin films were distinctive in showing that Fe-doping caused Ti^{4+} reduction, Mo-doping caused Ti^{4+} oxidation, and codoping did not alter the Ti valence. The XPS data also showed that the precursor valences of Fe^{3+} and Mo^{5+} were reduced upon annealing. Analysis of the potential roles of thermodynamics and intervalence charge transfer (IVCT) demonstrates that the latter drives the equilibria both in solution and during annealing. Photocatalytic performance testing indicated that Fe-doping was slightly deleterious, Mo doping had a consistent positive effect, and codoping exhibited a clear negative trend as a function of doping concentration. These results are interpreted in terms of the effect of IVCT on the matrix valence, dopant valences, and charge carrier trapping. Fe doping exhibited reduced performance because both matrix Ti$^{(4-x)+}$ and dopant Fe$^{(3-y)+}$ acted as electron traps. Mo doping exhibited enhanced performance because the matrix Ti$^{(4+x)+}$ acted as a hole trap and the dopant Mo$^{(5-x)+}$ and Mo$^{(4-x)+}$ acted as electron traps, thereby promoting charge separation. Codoping exhibited a clearly detected negative trend on the performance because, while Ti^{4+} played no role, Fe$^{(3-y)+}$, Mo$^{(5-x)+}$, and Mo$^{(4-x)+}$ all acted as traps for the majority charge carrier electrons.

Keywords Titania · Sol–gel · Thin film · Photocatalysis · Thermodynamics · Intervalence charge transfer

1 Introduction

There has been increasing focus on the development of renewable and clean energies based on solar power. Nanostructured semiconducting materials have been developed as potential solutions for the utilisation of solar energy for hydrogen production and the photodegradation of organic pollutants [1–3]. Although photocatalytic TiO$_2$ has been investigated extensively, its wide band gap and high electron–hole recombination rate have limited its applicability [4]. In order to improve the photocatalytic performance, doping has been investigated extensively

with the aim of improving the photoresponse under solar light [5–8].

One of the most common methods to improve these characteristics in semiconducting oxides is through the use of dopants. One of the most important of these parameters is the optical indirect band gap, which can be lowered by convergence of the conduction and valence band positions as well as the introduction of shallow midgap energy levels, which derive from the introduction of lattice defects [9], the presence of biaxial tension in the a–b plane of TiO$_2$ imposed by dopants [10], increasing the crystallinity [11], and/or activating intervalence charge transfer (IVCT) [11]. Another important parameter that can be

manipulated is extension of the electron–hole pair recombination time, which can be enhanced through the presence of deep midgap energy levels, which again derive from lattice defects [12]. Two other important parameters are charge carrier diffusion distance and density of surface-active sites, the effects of which can be enhanced through reductions in grain size [13, 14]. Finally, charge carrier mobility can be improved by reduction in scattering by lattice defects, grain boundaries, and surfaces [15].

Doping of TiO_2 using transition metal elements has attracted considerable interest as it has been shown to have the capacity to enhance the photocatalytic efficiency [16–24]. Of the various transition metal ions, Fe and Mo are of considerable interest owing to multiple valence states (Fe^{3+}, Fe^{2+}, Mo^{6+}, Mo^{5+}, Mo^{4+}) and the resultant potential for the imposition of different midgap defect energies and IVCT. Table 1 summarizes prior work on Fe or Mo single doped TiO_2.

However, there is only a limited amount of work that has been done on TiO_2 codoped with two transition metals [37–39], which enhances the capacity to increase charge transfer through intervalence charge transfer [40, 41]. Wang et al. [37] demonstrated that 0.10 mol% Fe/0.40 mol% Co codoped TiO_2 nanocrystals revealed the highest photoactivity under visible light, which was attributed to the promotion of charge carrier separation and interfacial charge transfer. Lin et al. [38] demonstrated that undoped TiO_2 thin films revealed the best photocatalytic performance relative to Fe/Mn codoped thin films, which was attributed to the increased density of recombination centres and the enhancement of lattice distortion. Chen et al. [39] observed that 0.05 mol% Co/0.05 mol% V

codoped TiO_2 thin film exhibited the best photocatalytic performance, which was attributed to modification of the band gap and associated semiconducting effects.

The present work reports the preparation of Fe/Mo codoped TiO_2 thin films by spin coating on polished fused silica glass substrates, followed by annealing at 450 °C for 2 h. The thin films were characterised by glancing angle X-ray diffraction (GAXRD), laser Raman microspectoscopy (Raman), atomic force microscopy (AFM), UV–Vis spectrophotometry (UV–Vis), and X-ray photoelectron spectrometry (XPS). The photocatalytic efficiency was determined comparatively in terms of methylene blue (MB) degradation under UV light for 24 h.

2 Experimental procedure

2.1 Sample fabrication

The fabrication process for TiO_2 thin films using spin coating has been described in detail elsewhere [42–44]. Polished fused silica substrates were selected because they risk contamination by only a single cation dopant and Si doping of TiO_2 has been reported to have a neutral or positive effect on the photocatalytic performance [45]. However, the most important study is that of Kabir et al. [46], who determined that Si contamination of TiO_2 thin films deposited and annealed on fused silica substrates derived solely from grain boundary diffusion. Consequently, the only effect was blockage of active sites rather than alteration of the defect state.

The fabrication procedures are detailed as follows:

Table 1 Survey of experimental work on Fe-doped and Mo-doped TiO_2 photocatalysts

Dopant	Type	Method	Doping levels	Light source	Efficiency	References
Fe	NPs	Hydrothermal	≤ 0.1 mol%	Visible (150 W)	93% in 3 h	[25]
		Sol–gel	≤ 10 wt%	UV (15 W) Visible (250 W)	58% in 5 h 44% in 5 h	[26]
		Sol–gel	≤ 10 mol%	Visible (500 W)	90% in 3 h	[27]
		Coprecipitation	≤ 5 wt%	UV (8 W) Visible (8 W)	85% in 1 h 20% in 1 h	[28]
		Sol–gel	≤ 5 wt%	UV (–)	84% in 2 h	[29]
		Coprecipitation	≤ 1 mol%	Visible (500 W)	85% in 0.5 h	[30]
	TFs	Precipitation	≤ 5 at%	Visible (500 W)	90% in 6 h	[31]
		Spin coating	≤ 1 mol%	UV (8 W)	47.5% in 24 h	Present work
Mo	NPs	Sol–gel	≤ 3 mol%	UV (250 W) Visible (250 W)	70% in 2.5 h 70% in 2.5 h	[32]
		Sol–gel	≤ 2 mol%	Visible (380 W)	100% in 6 min	[33]
	TFs	Spin coating	≤ 1 mol%	UV (8 W)	80.9% in 24 h	[34]
		Dip coating	≤ 0.2 wt%	UV (8 W)	90.6% in 24 h	[35]
		Spin coating	≤ 1 mol%	UV (8 W)	90% in 48 h	[36]
		Spin coating	≤ 1 mol%	UV (8 W)	54.4% in 24 h	Present work

NPs nanoparticles, *TFs* thin films

- *Precursor solutions*: Titanium tetraisopropoxide (TTIP, Reagent Grade, 97 wt%, Sigma-Aldrich) was dissolved in isopropanol (Reagent Plus, ≥ 99 wt%, Sigma-Aldrich) at 0.1 M titanium concentration.
- *Doping and codoping*: The Fe^{3+} or Mo^{5+} dopant level was varied in the range 0.00–0.10 mol% (metal basis) by adding $FeCl_3$ (Reagent Grade, 99 wt%, Sigma-Aldrich) and/or $MoCl_5$ (Reagent Grade, 95 wt%, Sigma-Aldrich) to the solution.
- *Mixing*: The precursor solution was mixed by manual stirring for 10 min in a Pyrex beaker without heating.
- *Repeat coating process*: Spin coating (Laurell Technologies WS-65052) was done by depositing ~ 0.2 mL of precursor solution onto a polished fused silica substrate spinning at 2000 rpm in nitrogen over a period of ~ 10 s. The films were dried by spinning for an additional 15 s and the overall process was repeated six more times (~ 1.4 mL), ultimately yielding films of thickness 300 ± 10 nm.
- *Annealing*: Annealing in air was done in a muffle furnace at 450 °C for 2 h; the heating rates were 0.5 °C/min from room temperature to 200 °C and 1 °C/min from 200 to 450 °C, followed by natural cooling.

2.2 Characterisation

The resultant films were characterised using the following techniques:

- Glancing angle X-ray diffraction (GAXRD; 45 kV, 40 mA, PANalytical Empyrean Thin-Film XRD).
- Laser Raman microspectroscopy (Raman; green argon ion laser (514 nm, 25 mW, 50X, spot size 1.5 mm, Renishaw inVia Raman Microscope).
- Atomic force microscopy (AFM; tapping mode, scan size 1 µm × 1 µm, Bruker Dimension Icon Scanning Probe Microscope).
- Ultraviolet–visible spectrophotometry (UV–Vis; dual-beam, 300–800 nm, PerkinElmer Lambda 35 UV–Visible Spectrophotometer).
- X-ray photoelectron spectroscopy (XPS; 20 °C, 10^{-7} Pa vacuum, 13 kV, 12 mA, spot size 500 mm, 2–5 nm beam penetration, Thermo Scientific ESCALAB 250Xi X-ray Photoelectron Spectrometer Microprobe).

2.3 Photocatalytic performance

The photocatalytic performances of the TiO_2 thin films were assessed in terms of photo-bleaching of methylene blue (MB) dye solutions, which has been described in detail elsewhere [42–44]. This testing was done by immersing each TiO_2 thin film in MB solution and then irradiating under UV light for 24 h. The MB solutions were prepared using methylene blue (M9140, dye content ≥ 82 wt%, Sigma-Aldrich) dissolved in deionized water at 10^{-5} M concentration. The solutions were magnetically stirred in a Pyrex beaker for 1 h without heating. The samples were placed in MB solution in a dark container for saturation for ~ 12 h prior to testing. The samples then were placed in separate small beakers filled with ~ 10 mL of MB solutions and exposed to UV radiation (3UV-38, 8 W, UVP) for 24 h. The vertical lamp-liquid and liquid-sample distances were ~ 6 cm and ~ 4 cm, respectively. After irradiation, the tested MB solutions were analysed by UV–Vis spectrophotometry in order to determine the extent of degradation.

3 Results and discussion

Figure 1 show the GAXRD patterns and Raman spectra, respectively, of the annealed undoped and doped thin films with varying doping concentrations. All of the thin films consist of anatase as the only crystalline phase. These data suggest that Fe or Mo doping causes only a slight reduction in the crystallinity (i.e., lattice stability) and that codoping has little or no effect.

Images of the topographies of the TiO_2 thin films are shown in Figs. 2, 3, and 4 and the associated data for the grain sizes and surface roughnesses are given in Table 2. These data show that there are few differences between the samples, so the data are not sufficiently distinctive to allow more than the conclusion that doping appears to increase the grain size marginally. An increase in grain growth upon doping is not unexpected as it is well known that defects enhance this.

Figure 5 shows the UV–Vis transmission spectra of the annealed doped TiO_2 thin films at varying doping concentrations. The films are flat and highly transparent and the absorption edges show no particular trends as a function of doping but there are significant blue shifts at the lower wavelengths, which are not advantageous.

Table 3 gives the optical indirect band gaps (E_g) of the doped TiO_2 thin films, which were calculated by the Tauc method [47]. These data suggest that doping causes a slight increase in the band gap, which is consistent with the blue shift of the absorption edges.

Surface chemical analysis by XPS has emerged as a standard tool in materials characterisation because it quantitatively identifies valence states [11, 35, 36]. Consequently, the peak shifts indicating valence increases (greater binding energies) and decreases (lower binding energies) provide information on charge transfer effects. In particular, electron transfer and complementary valence shifts between codopants, between dopant and matrix, and between codopants and matrix can be used to support the conclusion of IVCT [11, 39] or multivalence
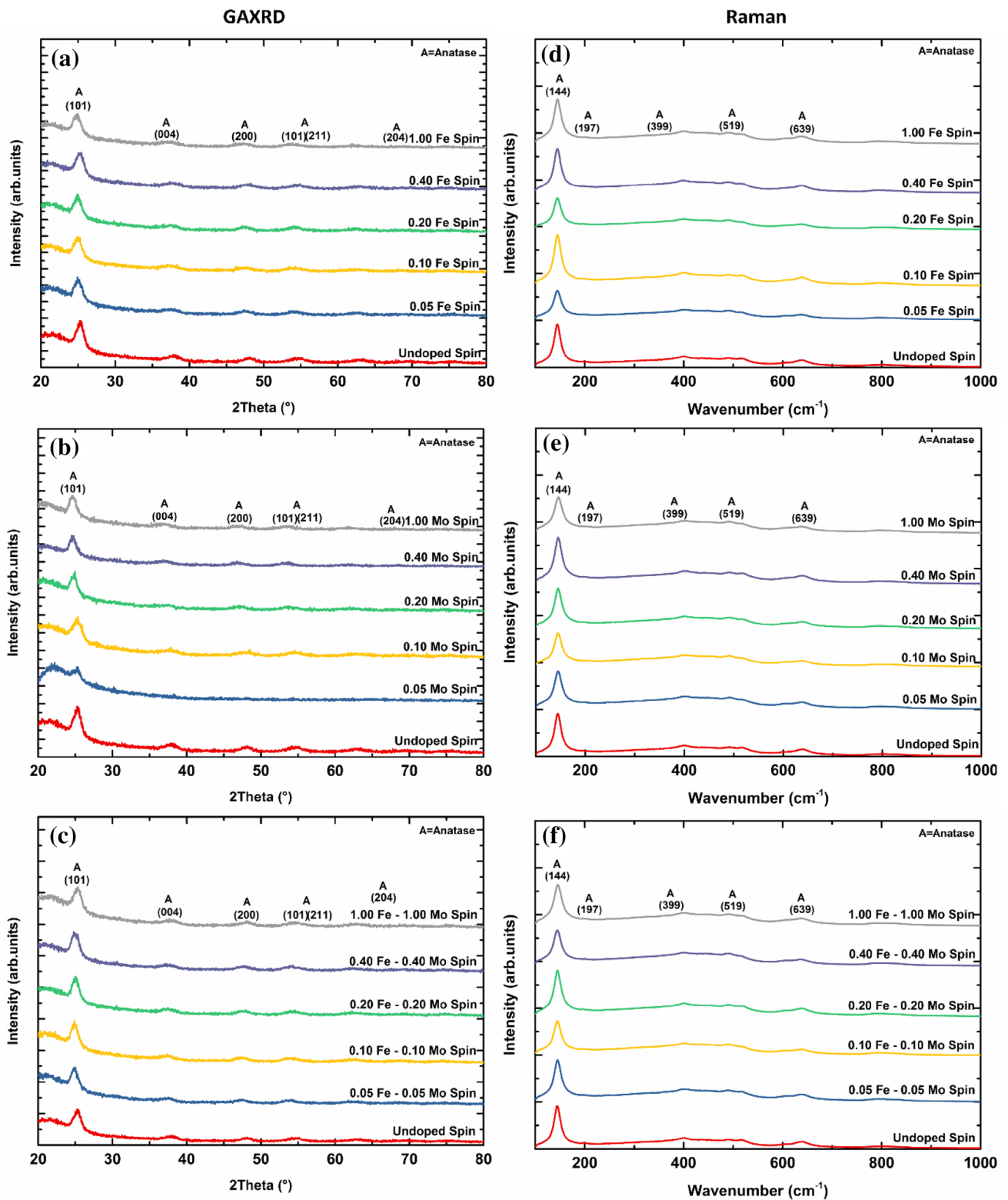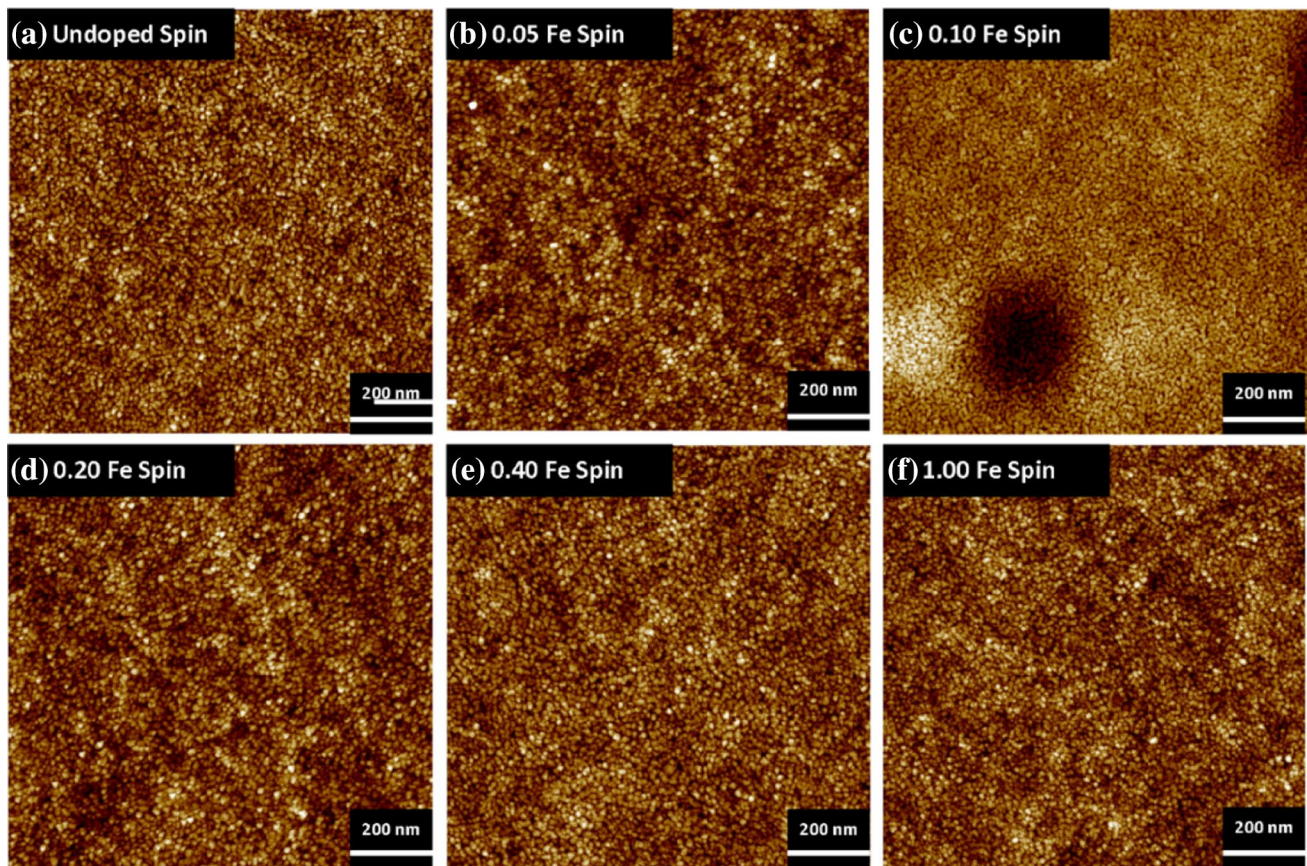
GAXRD   **Raman**

Fig. 1 GAXRD patterns (**a** Fe-doped, **b** Mo-doped, **c** Fe/Mo codoped) and Raman laser microspectra (**d** Fe-doped, **e** Mo-doped, **f** Fe/Mo codoped) of thin films annealed with varying doping levels at 450 °C for 2 h

Fig. 2 AFM images of Fe-doped TiO_2 thin films annealed with varying doping levels at 450 °C for 2 h

charge transfer (MVCT) [41]. In addition, these data can indicate the presence of direct redox effects, such as $2Ti^{4+} \rightarrow 2Ti^{3+} + V_O^{\cdot\cdot}$, where the latter is a charge compensating oxygen vacancy.

Figure 6 shows the XPS spectra for the annealed doped TiO_2 thin films at the different doping concentrations. In Fig. 6a, the two main Ti2p peaks for TiO_2 at 458.30 eV ($Ti2p_{3/2}$) and 464.05 eV ($Ti2p_{1/2}$) confirm the presence of Ti^{4+} [48, 49]. It can be seen that Fe-doping caused the binding energies to decrease (indicating Ti^{4+} valence decrease), Mo-doping caused the binding energy to increase (indicating Ti^{4+} valence increase), and the codoping did not change the Ti valence.

In Fig. 6b, c, the two main Fe2p peaks at ~710.0 eV (Fe2p3/2) and ~723.5 eV (Fe2p1/2) suggest the presence of $Fe^{3+/2+}$ [50] for both Fe-doping and codoping. Although the Fe^{3+} and Fe^{2+} peaks cannot be differentiated due to overlap, there appears to be shifts to lower binding energies relative to the Fe^{3+} precursor, suggesting decreases in valence for both doping types. In contrast, Fe^{3+} is thermodynamically more likely to be present in the films after annealing at 450 °C in air [38], so a shift to higher binding energy would be expected.

In Fig. 6d, e, the two main Mo3d peaks represent Mo_2O_5 at 232.18 eV (Mo3d5/2) and 235.28 eV (Mo3d3/2) [32, 51], and Mo_2O_4 at 230.56 eV and 233.78 eV [36] for both Mo-doping and codoping. It is clear that some of the Mo^{5+} has reduced to Mo^{4+} but the presence of the most thermodynamically stable Mo^{6+} valence is not certain as the shoulder on the Mo^{5+} is not unambiguous. As Mo^{5+} is not thermodynamically stable after annealing at 450 °C in air [36], its conversion to Mo^{4+} and possibly Mo^{6+} would be expected.

The preceding suggests that the processes of dissolution and partial equilibration may be influenced by both thermodynamics and IVCT. Figure 7 shows the Gibbs standard free energies, which are available, for the stepwise oxidation reactions for the dopants and matrix as a function of temperature. These data indicate that $Fe^{2+} \rightarrow Fe^{3+}$ oxidation is favoured over $Ti^{3+} \rightarrow Ti^{4+}$ oxidation, so the thermodynamics of the Fe–O system will dominate those of the Ti–O system. In contrast, for Fe-doping by precursor Fe^{3+}, the XPS data indicate valence decreases (i.e., reduction) for both Ti and Fe. Since the Gibbs free energies of reaction at 450 °C for $Fe_2O_3 \rightarrow 2FeO + 1.5O_2$ (+184.8 kJ/mol) and $TiO_2 \rightarrow 0.5Ti_2O_3 + 0.25O_2$ (+155.6 kJ/mol) are positive,
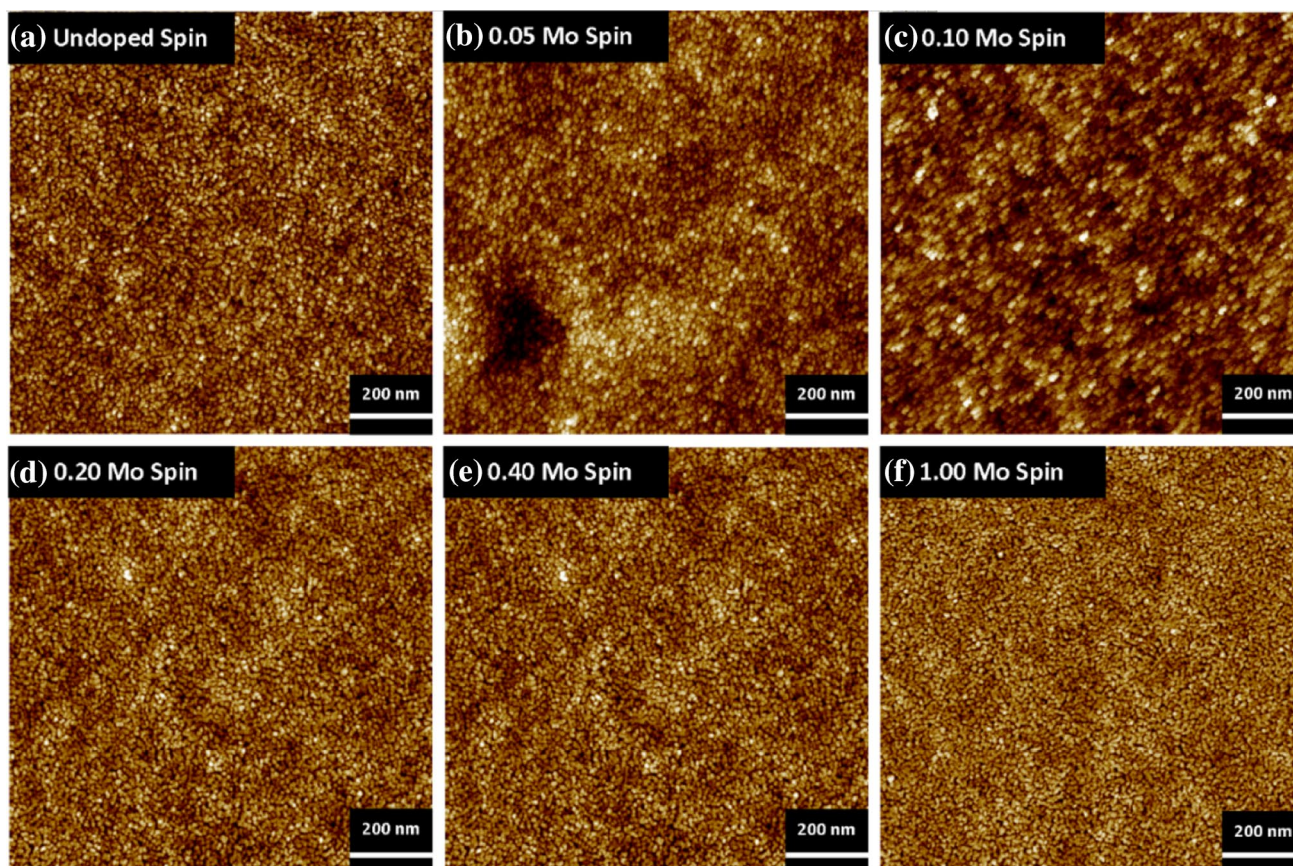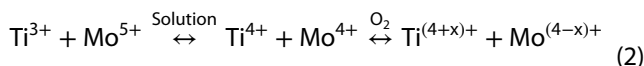
Fig. 3 AFM images of Mo-doped TiO$_2$ thin films annealed with varying doping levels at 450 °C for 2 h

neither is favoured thermodynamically. This contradiction between the XPS data and thermodynamics can be explained by IVCT, as indicated in Reaction 1 (where Ti^{3+} is the minority species). Following IVCT, which alters the balance of the valences in solution, the final valences are equilibrated during annealing, which effectively results in reduced valence states for the dominant species in both matrix (Ti^{4+}) and dopant (Fe^{3+}) relative to the precursors, thereby matching the XPS data. As these are contrary to the free energy calculations for oxidation at 450 °C, then IVCT drives the equilibria both in solution and during annealing.

$$Ti^{3+} + Fe^{3+} \overset{Solution}{\leftrightarrow} Ti^{4+} + Fe^{2+} \overset{O_2}{\leftrightarrow} Ti^{(4-x)+} + Fe^{(2+x)+} \quad (1)$$
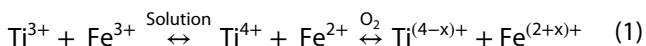
For Mo-doping by precursor Mo^{5+}, assuming that Mo^{6+} is not formed, the XPS data indicate a valence increase (i.e., oxidation) for Ti and a valence decrease (i.e., reduction) for Mo. Since the thermodynamic stability diagram for Mo–O [36] shows that neither Mo^{5+} nor Mo^{3+} are stable and Fig. 1 does not provide useful data for this system, then the driving force for redox in solution could be either thermodynamics (as Ti$^{3+} \rightarrow$ Ti^{4+} oxidation is favoured) and/or IVCT (the mechanism alternative to thermodynamics).

These are given in Reaction 2, which matches the XPS data. It is concluded that the equilibria during annealing are driven by IVCT because the majority Ti$^{4+} \rightarrow$ Ti^{5+} oxidation is not thermodynamically favoured as is the case for Mo$^{5+} \rightarrow$ Mo^{4+} reduction.

$$Ti^{3+} + Mo^{5+} \overset{Solution}{\leftrightarrow} Ti^{4+} + Mo^{4+} \overset{O_2}{\leftrightarrow} Ti^{(4+x)+} + Mo^{(4-x)+} \quad (2)$$

However, although the XPS data are ambiguous, it is possible that Mo^{6+} is formed, as suggested by a thermodynamic modelling study that indicated MoO$_3$ stability at temperatures up to ~850 °C. Accordingly, Reaction 3 also matches the XPS data, where the Mo^{5+} peaks shift to lower binding energies. This supports the conclusion that Mo^{6+} is not formed because, while Reaction 3 gives the only feasible valence conversions, the majority Ti$^{4+} \rightarrow$ Ti^{5+} oxidation is not thermodynamically favoured and IVCT does not generate Mo^{6+} as a final reaction product.

$$Ti^{4+} + Mo^{5+} \overset{Solution}{\leftrightarrow} Ti^{3+} + Mo^{6+} \overset{O_2}{\leftrightarrow} Ti^{(4+x)+} + Mo^{(5-x)+} \quad (3)$$
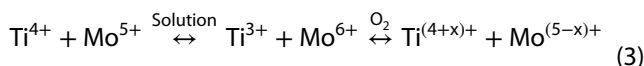
For codoping, the XPS data indicate effectively no valence change for Ti but valence decreases (i.e.,
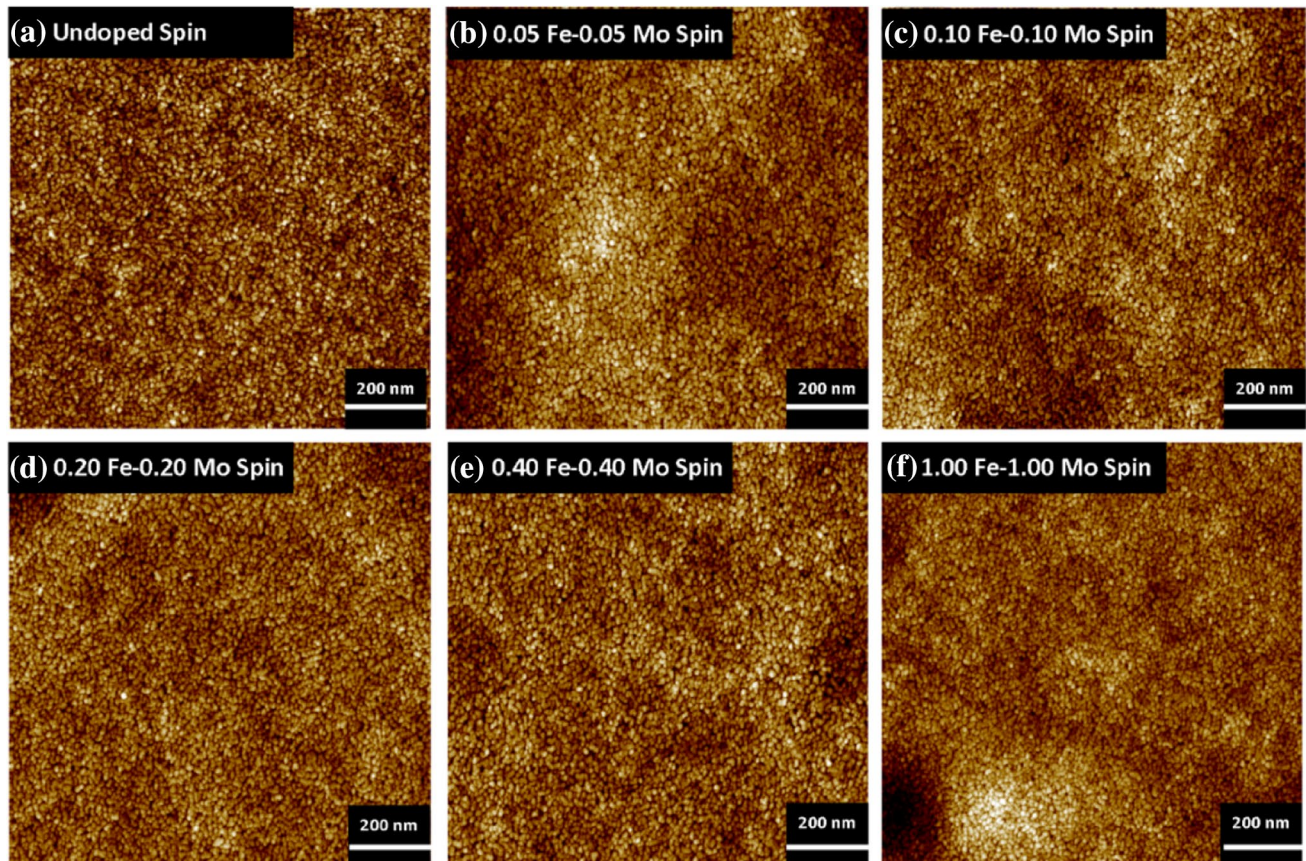
Fig. 4 AFM images of Fe/Mo codoped TiO_2 thin films annealed with varying doping levels at 450 °C for 2 h

Table 2 Variation in grain sizes and surface roughnesses of annealed doped TiO_2 thin films based on AFM data

Single doping						
	Undoped	0.05 Fe	0.10 Fe	0.20 Fe	0.40 Fe	1.00 Fe
Grain size (nm)	12.9	15.0	14.5	16.0	14.7	14.1
Surface roughness (nm)	0.923	0.672	0.879	0.695	0.888	0.603
	Undoped	0.05 Mo	0.10 Mo	0.20 Mo	0.40 Mo	1.00 Mo
Grain size (nm)	12.9	12.5	15.1	16.4	15.2	13.6
Surface roughness (nm)	0.923	2.350	3.570	1.370	0.915	1.110
Codoping						
	Undoped	0.05 Fe–0.05 Mo	0.10 Fe–0.10 Mo	0.20 Fe–0.20 Mo	0.40 Fe–0.40 Mo	1.00 Fe–1.00 Mo
Grain size (nm)	12.9	15.2	13.5	14.4	15.9	16.6
Surface roughness (nm)	0.923	1.080	1.090	1.130	0.947	0.963

reduction) for both Fe and Mo, again unfavourable thermodynamically. This situation cannot be assessed unambiguously because any shifts in the deconvoluted XPS peaks for Mo^{4+} cannot be determined and there are no thermodynamic data for Mo_2O_5 or Mo_2O_3, which are relevant to the reactions $Mo_2O_5 \rightarrow 2MoO_2 + 0.5O_2$ or $MoO_2 \rightarrow 0.5Mo_2O_3 + 0.25O_2$. Since Mo^{5+} and Mo^{3+} do not appear to be thermodynamically stable [36], the first reaction would be favoured but the second wouldn't. Nonetheless, Reaction 4 harmonises the XPS data by illustrating
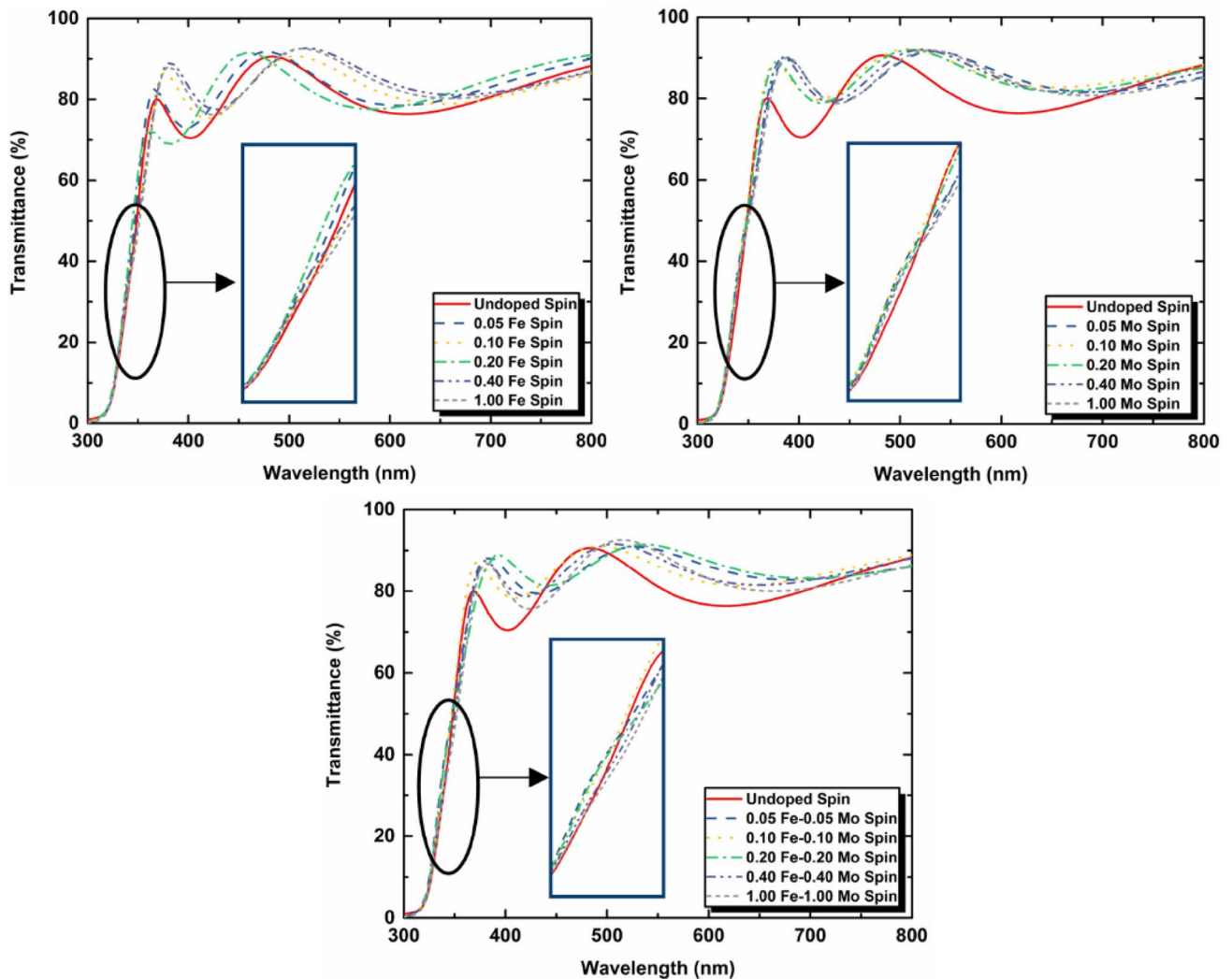
Fig. 5 UV–Vis transmission spectra of thin films annealed with varying doping levels at 450 °C for 2 h

Table 3 Optical indirect band gaps of annealed doped TiO_2 thin films

Single doping						
	Undoped	0.05 Fe	0.10 Fe	0.20 Fe	0.40 Fe	1.00 Fe
Optical indirect band gap (eV)	3.40	3.41	3.45	3.42	3.45	3.43
	Undoped	0.05 Mo	0.10 Mo	0.20 Mo	0.40 Mo	1.00 Mo
Optical indirect band gap (eV)	3.40	3.45	3.43	3.43	3.43	3.43
Codoping						
	Undoped	0.05 Fe−0.05 Mo	0.10 Fe−0.10 Mo	0.20 Fe−0.20 Mo	0.40 Fe−0.40 Mo	1.00 Fe−1.00 Mo
Optical indirect band gap (eV)	3.40	3.48	3.43	3.42	3.43	3.40

that, relative to the precursors, IVCT between matrix and dopant drives the reaction in solution (since Fe reduction at room temperature is not favoured thermodynamically) but IVCT between dopants drives the reaction during annealing (since neither dopant valence is favoured thermodynamically):
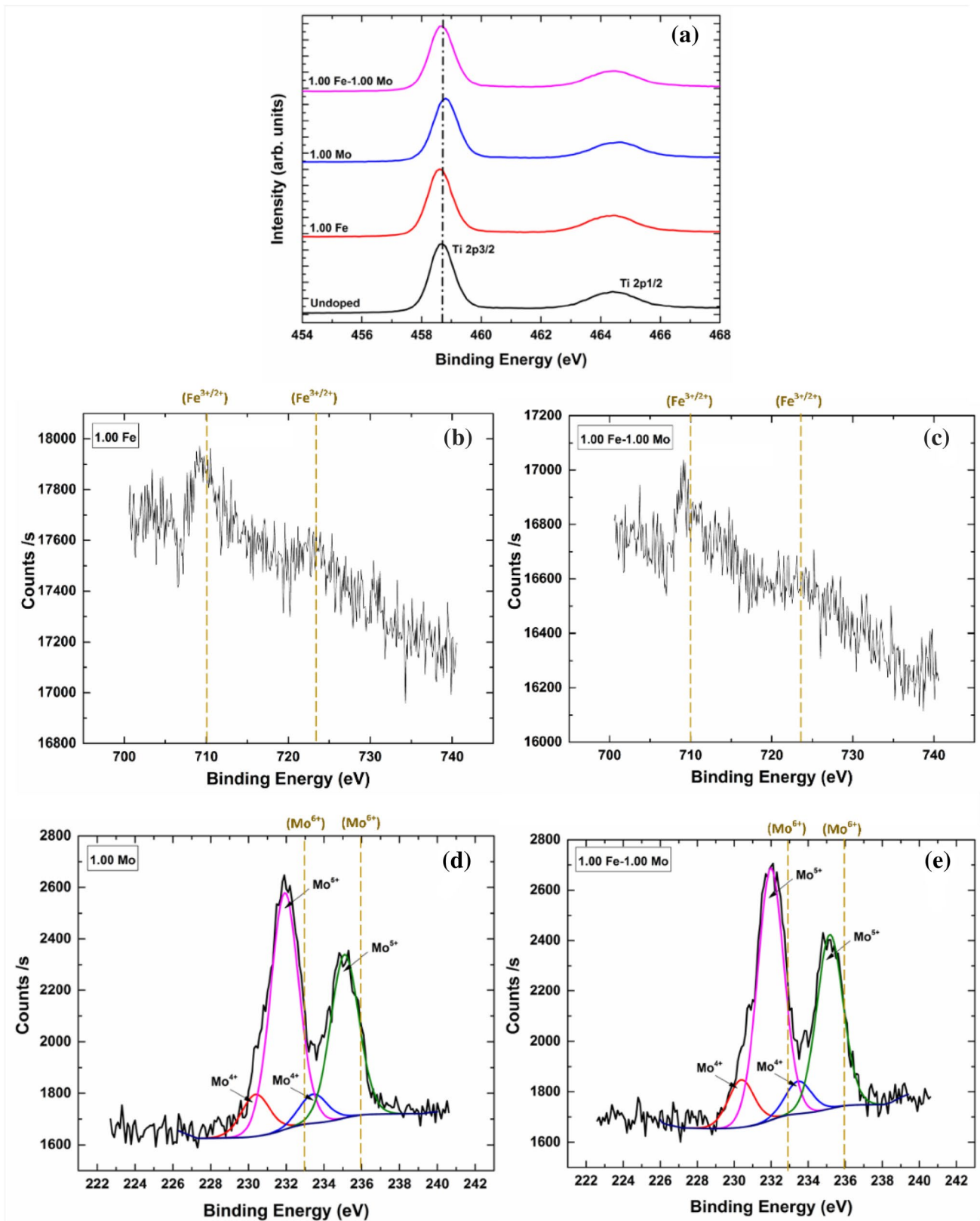
Fig. 6 **a** Ti2p, **b**, **c** Fe2p, and **d**, **e** Mo3d XPS spectra for 1.00 mol% doped thin films annealed with varying doping levels at 450 °C for 2 h
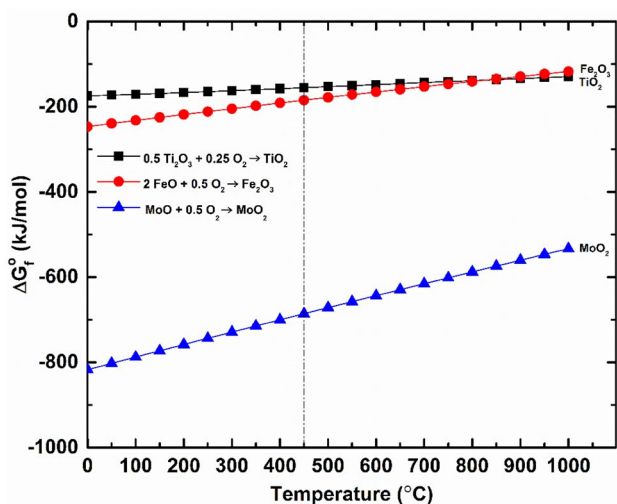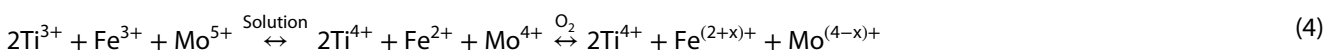
Fig. 7 Gibbs standard free energies for stepwise oxidation reactions of dopants and matrix as a function of temperature

scales of electronegativities of Ti matrix and Fe and Mo dopants. These data tend to show that the electronegativities of dopants are the greater value than that of the Ti matrix, indicating that the electron cloud of the O in the Mo–O–Ti and Fe–O–Ti bonding configuration would move toward that of dopants, causing Fe and Mo valences to increase and that of Ti to decrease. However, it is unlikely that electronegativity plays a significant role since the Ti valence decreases only with Fe doping of TiO_2.

For size considerations, the crystal radii of Ti, Fe, and Mo in sixfold (substitutional) and fivefold (interstitial) coordinations [60] are given in Table 5. According to Hume-Rothery's rules for substitutional solid solubility [36], it is very likely that this type of solid solubility occurred owing to the similar crystal radii of Ti^{4+}, Fe^{4+}, Fe^{3+} (high spin), Fe^{2+} (low spin) for Fe-doping, and Mo^{6+}, Mo^{5+}, Mo^{4+} and Mo^{3+} for Mo-doping. However, it also is possible that interstitial solid solubility occurred since each of the two interstices adjacent to the central Ti in the elongated TiO_6 octahedron of anatase has a radius of 0.0782 nm [11]; Fe^{4+}, Fe^{3+} (low

$$2Ti^{3+} + Fe^{3+} + Mo^{5+} \overset{Solution}{\longleftrightarrow} 2Ti^{4+} + Fe^{2+} + Mo^{4+} \overset{O_2}{\longleftrightarrow} 2Ti^{4+} + Fe^{(2+x)+} + Mo^{(4-x)+} \tag{4}$$

An alternative approach is consideration of the effect of electronegativity [52]. Table 4 summarises the different

spin), and Mo^{6+} can fit in this position. According to the crystal field stabilisation energies, Fe^{3+} and Fe^{2+} are likely

Table 4 Summary of electronegativities of Ti, Fe, and Mo in different scales

Scale References	Allen [53]	Allred–Rochow [54]	Little, Jr. [55]	Mulliken [56]	Pauling [57]	Pearson [58]	Sanderson [59]
Ti	1.38	1.32	1.32	5.2	1.54	3.45	1.50
Fe	1.80	1.64	1.64	6.06	1.83	4.06	2.20
Mo	1.47	1.30	1.30	7.04	2.16	3.90	2.20

Table 5 Relevant Shannon crystal radii in sixfold and fivefold coordinations [60]

Cation	Coordination	Valence	Spin	Crystal radius (nm)	Radius difference with Ti^{4+} in sixfold coordination (%)
Ti	VI	4+	–	0.0745	–
		3+	–	0.081	+ 8.72
		2+	–	0.100	+ 34.23
Fe		4+	–	0.0725	− 2.68
		3+	Low	0.069	− 7.38
			High	0.0785	+ 5.37
		2+	Low	0.075	+ 0.67
			High	0.092	+ 23.49
Mo		6+	–	0.073	− 2.01
		5+	–	0.075	+ 0.67
		4+	–	0.079	+ 6.04
		3+	–	0.083	+ 11.41
Ti	V	4+	–	0.065	N/A
Fe		3+	–	0.072	N/A
Mo		6+	–	0.064	N/A

to be high-spin complexes [36]. For the latter case, Fe^{2+} is unlikely to be soluble, which suggests that the $Fe^{(2+x)+}$ of Reactions 1 and 3 is more appropriately represented at $Fe^{(3-x)+}$ in terms of the size of x, which would be small.

The potential dopant effects on defect equilibria, using Kröger–Vink notation [61], that can arise from doping with Fe or Mo are summarised in Table 6. The defects in the form of oxygen vacancies, metal substitutionals, metal interstitials, and metal vacancies would provide midgap states, which could have the capacity to improve the photocatalytic performance. With electron charge compensation, the electron and hole charge carriers are subject to traps in the form of the defects, which could have the capacity to increase the charge separation and carrier lifetime.
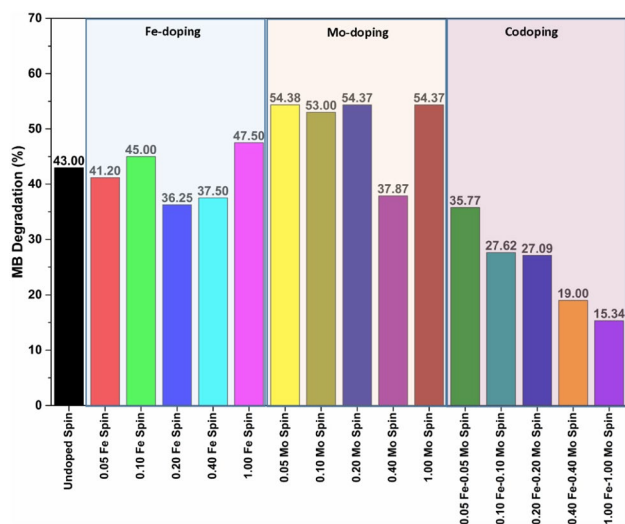
Figure 8 shows the photocatalytic performances of the undoped and doped TiO_2 thin films evaluated by photobleaching of MB solution for 24 h. The performances of the Fe-doped TiO_2 thin films generally were slightly inferior to that of the undoped sample while the performance of the Mo-doped TiO_2 thin films generally were superior to that of the undoped sample. For the codoped TiO_2 thin films, the performances were more consistent in revealing the degradation in performance in proportion to the codoping concentration.

Considering the three sets of data globally, the performance data do not correlate with the degrees of crystallinity (Fig. 1), absorption edge, indirect band gap (Fig. 5 and Table 3), or microstructure (Figs. 2, 3, 4). In more conventional thought, which would consider oxygen vacancy formation, only Fe doping would create oxygen vacancies in TiO_{2-x}, which would be expected to enhance the photocatalytic performance. However, Fig. 4 shows that this was not the case. Considering the formation of midgap states, both Fe and Mo doping have the capacity to reduce the band gap, but Table 3 shows that, again, this was not the case. Since all of these typically key factors do not appear to be dominant, then this suggests the importance of the valences as revealed by the XPS data:

Table 6 Potential dopant effects on defect equilibria

Ion	Solid solubility	Charge compensation	Defect equilibria
Fe	Substitutional	Ionic	$FeO \rightarrow Fe''_{Ti} + V^{\cdot\cdot}_O + O^x_O$
			$Fe_2O_3 \rightarrow 2Fe'_{Ti} + V^{\cdot\cdot}_O + 3O^x_O$
		Electronic	$FeO + \frac{1}{2}O_2(g) \rightarrow Fe''_{Ti} + 2h^{\cdot} + 2O^x_O$
			$Fe_2O_3 + \frac{1}{2}O_2(g) \rightarrow 2Fe'_{Ti} + 2h^{\cdot} + 4O^x_O$
	Interstitial	Ionic	$2FeO \rightarrow 2Fe^{\cdot\cdot}_i + V''''_{Ti} + 2O^x_O$
			$2Fe_2O_3 \rightarrow 4Fe^{\cdot\cdot\cdot}_i + 3V''''_{Ti} + 6O^x_O$
		Electronic	$FeO + \frac{1}{2}O_2(g) \rightarrow Fe^{\cdot\cdot}_i + 2e' + 2O^x_O$
			$Fe_2O_3 + \frac{1}{2}O_2(g) \rightarrow 2Fe^{\cdot\cdot\cdot}_i + 6e' + 4O^x_O$
Mo	Substitutional	Ionic	$2MoO_3 \rightarrow 2Mo^{\cdot\cdot}_{Ti} + V''''_{Ti} + 6O^x_O$
			$2Mo_2O_5 \rightarrow 4Mo^{\cdot}_{Ti} + V''''_{Ti} + 10O^x_O$
			$MoO_2 \rightarrow Mo^x_{Ti} + 2O^x_O$
			$Mo_2O_3 \rightarrow 2Mo'_{Ti} + V^{\cdot\cdot}_O + 3O^x_O$
			$MoO \rightarrow Mo''_{Ti} + V^{\cdot\cdot}_O + O^x_O$
		Electronic	$MoO_3 + V^{\cdot\cdot}_o \rightarrow Mo^{\cdot\cdot}_{Ti} + 2O^x_O$
			$Mo_2O_5 + V^{\cdot\cdot}_o \rightarrow 2Mo^{\cdot}_{Ti} + 4O^x_O$
			$MoO_2 \rightarrow Mo^x_{Ti} + 2O^x_O$
			$Mo_2O_3 + \frac{1}{2}O_2(g) \rightarrow 2Mo'_{Ti} + 2h^{\cdot} + 4O^x_O$
			$MoO + \frac{1}{2}O_2(g) \rightarrow Mo^{\cdot\cdot}_i + 2e' + 2O^x_O$
	Interstitial	Ionic	$2MoO_3 \rightarrow 2Mo^{\cdot\cdot\cdot\cdot\cdot\cdot}_i + 3V''''_{Ti} + 6O^x_O$
			$2Mo_2O_5 \rightarrow 4Mo^{\cdot\cdot\cdot\cdot\cdot}_i + 5V''''_{Ti} + 10O^x_O$
			$MoO_2 \rightarrow Mo^{\cdot\cdot\cdot\cdot}_i + V''''_{Ti} + 2O^x_O$
			$2Mo_2O_3 \rightarrow 4Mo^{\cdot\cdot\cdot}_i + 3V''''_{Ti} + 6O^x_O$
			$2MoO \rightarrow 2Mo^{\cdot\cdot}_i + V''''_{Ti} + 2O^x_O$
		Electronic	$MoO_3 + V^{\cdot\cdot}_o \rightarrow Mo^{\cdot\cdot\cdot\cdot\cdot\cdot}_i + 4e' + 2O^x_O$
			$Mo_2O_5 + V^{\cdot\cdot}_o \rightarrow 2Mo^{\cdot\cdot\cdot\cdot\cdot}_i + 8e' + 4O^x_O$
			$MoO_2 \rightarrow Mo^{\cdot\cdot\cdot\cdot}_i + 4e' + 2O^x_O$
			$Mo_2O_3 + \frac{1}{2}O_2(g) \rightarrow 2Mo^{\cdot\cdot\cdot}_i + 6e' + 4O^x_O$
			$MoO + \frac{1}{2}O_2(g) \rightarrow Mo^{\cdot\cdot}_i + 2e' + 2O^x_O$

Fig. 8 Degradation of MB solutions photocatalysed for 24 h by thin films annealed with varying doping levels at 450 °C for 2 h

- *Fe doping*: The presence of $Ti^{(4-x)+}$ and $Fe^{(2+x)+}$ reflects $Ti^{4+} \rightarrow Ti^{3+}$ and $Fe^{3+} \rightarrow Fe^{2+}$ reductions (IVCT leaves the oxygen vacancy concentration unaffected), where $Ti^{(4-x)+}$ and $Fe^{(2+x)+}$ (effectively $Fe^{(3-y)+}$, where $y = 1 - x$) would act as an electron traps, resulting in diminished performance since TiO_2 is an *n*-type semiconductor and the principal charge carrier is electrons [62].

- *Mo doping*: The presence of $Ti^{(4+x)+}$, $Mo^{(5-x)+}$, and $Mo^{(4-x)+}$ reflects $Ti^{4+} \rightarrow Ti^{5+}$ oxidation and $Mo^{5+} \rightarrow Mo^{4+}$ reduction, where the majority $Ti^{(4+x)+}$ would act as a hole trap and minority $Mo^{(5-x)+}$ and $Mo^{(4-x)+}$ would act as electron traps. These valences would serve as effective hole traps while decreasing the majority electron charge carriers to a much lower extent. This would result in enhanced performance owing to increased charge separation.

- *Codoping*: The Ti valence is unchanged at Ti^{4+} but the dopants are converted from Fe^{3+} to $Fe^{(2+x)+}$ (effectively $Fe^{(3-y)+}$) and from Mo^{5+} to $Mo^{(5-x)+}$ and $Mo^{(4-x)+}$. Hence, Ti^{4+} would play no role in charge carrier trapping but all of the dopants would act as electron traps, so their combination would increase both the deleterious effect of codoping and the ability to detect it.

4 Conclusions

Fe/Mo single doped and codoped TiO_2 thin films were spin coated on polished fused silica substrates and annealed in air at 450 °C for 2 h. All of the thin films consisted of anatase; doping appeared to have only a slight negative effect on the crystallinity. There were few differences in grain sizes, with only a slight increase for the doped thin films. The thin films were flat and highly transparent,

where doping caused a slight blue shift and associated increase in E_g. The XPS data were distinctive in showing that Fe-doping caused Ti^{4+} reduction, Mo-doping caused Ti^{4+} oxidation, and codoping did not alter the Ti valence. The XPS data also showed that the precursor valences of Fe^{3+} and Mo^{5+} were reduced upon annealing. Of the thermodynamically stable valences Mo^{4+} and Mo^{6+}, the former was a final reaction product but it is unlikely that the latter was formed.

Analysis of the potential roles of thermodynamics and IVCT shows conclusively that the latter drives the equilibria both in solution and during annealing for all three types of doping. Photocatalytic performance testing indicated that Fe-doping was slightly deleterious, Mo doping had a consistent positive effect, and codoping exhibited a clear negative trend as a function of doping concentration. The data do not support the conclusion that crystallinity, microstructure, band gap, or midgap states played a dominant role in the photocatalytic performance. These results are interpreted in terms of the effect of IVCT on the matrix valence, dopant valences, and charge carrier trapping. Fe doping exhibited reduced performance because both matrix $Ti^{(4-x)+}$ and dopant $Fe^{(3-y)+}$ acted as electron traps. Mo doping exhibited enhanced performance because the matrix $Ti^{(4+x)+}$ acted as a hole trap and the dopant $Mo^{(5-x)+}$ and $Mo^{(4-x)+}$ acted as electron traps, thereby promoting charge separation. The role of IVCT was shown most distinctly through the negative trend that codoping had on the photocatalytic performance. Here, Ti^{4+} played no role but $Fe^{(3-y)+}$, $Mo^{(5-x)+}$, and $Mo^{(4-x)+}$ all acted as traps for the majority charge carrier electrons. This explains both why the trend occurred and why it was clearly detectable.

Compliance with ethical standards

Conflict of interest The authors declare that they have no conflict of interest.

References

1. Sakthivel S, Neppolian B, Shankar MV, Arabindoo B, Palanichamy M, Murugesan V (2003) Solar photocatalytic degradation of azo dye: comparison of photocatalytic efficiency of ZnO and TiO_2. Sol Energy Mater Sol Cells 77(1):65–82
2. Kwon YT, Song KY, Lee WI, Choi GJ, Do YR (2000) Photocatalytic behaviour of WO_3-loaded TiO_2 in an oxidation reaction. J Catal 191(1):192–199

3. Ao CH, Lee SC (2005) Indoor air purification by photocatalyst TiO_2 immobilized on an activated carbon filter installed in an air cleaner. Chem Eng Sci 60(1):103–109

4. Iwasaki M, Hara M, Kawada H, Tada H, Ito S (2000) Cobalt ion-doped TiO_2 photocatalyst response to visible light. J Colloid Interface Sci 224(1):202–204

5. Kiriakidou F, Kondarides DI, Verykios XE (1999) The effect of operational parameters and TiO_2-doping on the photocatalytic degradation of azo-dyes. Catal Today 54(1):119–130

6. Asahi R, Morikawa T, Ohwaki T, Aoki K, Taga Y (2001) Visible-light photocatalysis in nitrogen-doped titanium oxides. Science 293(5528):269–271

7. Ohno T, Akiyoshi M, Umebayashi T, Asai K, Mitsui T, Matsumura M (2004) Preparation of S-doped TiO_2 photocatalysts and their photocatalytic activities under visible light. Appl Catal A 265(1):115–121

8. Ohno T, Mitsui T, Matsumura M (2003) Photocatalytic activity of S-doped TiO_2 photocatalyst under visible light. Chem Lett 32(4):364–365

9. Baruah S, Rafique RF, Dutta J (2008) Visible light photocatalysis by tailoring crystal defects in zinc oxide nanostructures. Nano 3(05):399–407

10. Sun Y, Thompson SE, Nishida T (2007) Physics of strain effects in semiconductors and metal-oxide-semiconductor field-effect transistors. J Appl Phys 101(10):104503

11. Chen W-F, Koshy P, Huang Y, Adabifiroozjaei E, Yao Y, Sorrell CC (2016) Effects of precipitation, liquid formation, and inter-valence charge transfer on the properties and photocatalytic performance of cobalt-or vanadium-doped TiO_2 thin films. Int J Hydrogen Energy 41(42):19025–19056

12. Chen X, Liu L, Peter YY, Mao SS (2011) Increasing solar absorption for photocatalysis with black hydrogenated titanium dioxide nanocrystals. Science 331:746–749

13. Choi W, Termin A, Hoffmann MR (1994) The role of metal ion dopants in quantum-sized TiO_2: correlation between photoreactivity and charge carrier recombination dynamics. J Phys Chem 98(51):13669–13679

14. Xin B, Jing L, Ren Z, Wang B, Fu H (2005) Effects of simultaneously doped and deposited Ag on the photocatalytic activity and surface states of TiO_2. J Phys Chem B 109(7):2805–2809

15. Niemelä JP, Hirose Y, Hasegawa T, Karppinen M (2015) Transition in electron scattering mechanism in atomic layer deposited Nb:TiO_2 thin films. Appl Phys Lett 106(4):042101

16. Zhao Y, Li C, Liu X, Gu F, Du HL, Shi L (2008) Zn-doped TiO_2 nanoparticles with high photocatalytic activity synthesized by hydrogen–oxygen diffusion flame. Appl Catal B 79:208–215

17. Mirkhani V, Tangestaninejad S, Moghadam M, Habibi MH, Rostami-Vartooni A (2009) Photocatalytic degradation of azo dyes catalyzed by Ag doped TiO_2 photocatalyst. J Iran Chem Soc 6(3):578–587

18. Hu Y, Song X, Jiang S, Wei C (2015) Enhanced photocatalytic activity of Pt-doped TiO_2 for NO_x oxidation both under UV and visible light irradiation: a synergistic effect of lattice Pt^{4+} and surface PtO. Chem Eng J 274:102–112

19. Colon G, Maicu M, Hidalgo MS, Navio JA (2006) Cu-doped TiO_2 systems with improved photocatalytic activity. Appl Catal B 67(1–2):41–51

20. Khan M, Cao W (2013) Preparation of Y-doped TiO_2 by hydrothermal method and investigation of its visible light photocatalytic activity by the degradation of methylene blue. J Mol Catal 376:71–77

21. Gao B, Lim TM, Subagio DP, Lim TT (2010) Zr-doped TiO_2 for enhanced photocatalytic degradation of bisphenol A. Appl Catal A 375(1):107–115

22. Chang SM, Hou CY, Lo PH, Chang CT (2009) Preparation of phosphated Zr-doped TiO_2 exhibiting high photocatalytic activity through calcination of ligand-capped nanocrystals. Appl Catal B 90(1–2):233–241

23. Chen W-F, Mofarah SS, Hanaor DAH, Koshy P, Chen H-K, Jiang Y, Sorrell CC (2018) Enhancement of Ce/Cr codopant Solubility and chemical homogeneity in TiO_2 nanoparticles through sol–gel versus pechini syntheses. Inorg Chem 57(12):7279–7289

24. Hanaor DAH, Triani G, Sorrell CC (2011) Morphology and photocatalytic activity of highly oriented mixed phase titanium dioxide thin films. Surf Coat Technol 205(12):3658–3664

25. Sood S, Umar A, Mehta SK, Kansal SK (2015) Highly effective Fe-doped TiO_2 nanoparticles photocatalysts for visible-light driven photocatalytic degradation of toxic organic compounds. J Colloid Interface Sci 450:213–223

26. Moradi H, Eshaghi A, Hosseini SR, Ghani K (2016) Fabrication of Fe-doped TiO_2 nanoparticles and investigation of photocatalytic decolorization of reactive red 198 under visible light irradiation. Ultrason Sonochem 32:314–319

27. Ali T, Tripathi P, Azam A, Raza W, Ahmed AS, Ahmed A, Muneer M (2017) Photocatalytic performance of Fe-doped TiO_2 nanoparticles under visible-light irradiation. Mater Res Express 4(1):015022

28. Banisharif A, Khodadadi AA, Mortazavi Y, Firooz AA, Beheshtian J, Agah S, Menbari S (2015) Highly active Fe_2O_3-doped TiO_2 photocatalyst for degradation of trichloroethylene in air under UV and visible light irradiation: experimental and computational studies. Appl Catal B 165:209–221

29. Crişan M, Răileanu M, Drăgan N, Crişan D, Ianculescu A, Niţoi I, Oancea P, Şomăcescu S, Stănică N, Vasile B, Stan C (2015) Sol–gel iron-doped TiO_2 nanopowders with photocatalytic activity. Appl Catal A 504:130–142

30. Ma J, He H, Liu F (2015) Effect of Fe on the photocatalytic removal of NO_x over visible light responsive Fe/TiO_2 catalysts. Appl Catal B 179:21–28

31. Li J, Ren D, Wu Z, Xu J, Bao Y, He S, Chen Y (2018) Flame retardant and visible light-activated Fe-doped TiO_2 thin films anchored to wood surfaces for the photocatalytic degradation of gaseous formaldehyde. J Colloid Interface Sci 530:78–87

32. Wang S, Bai LN, Sun HM, Jiang Q, Lian JS (2013) Structure and photocatalytic property of Mo-doped TiO_2 nanoparticles. Powder Technol 244:9–15

33. Khan H, Berk D (2014) Synthesis, physicochemical properties and visible light photocatalytic studies of molybdenum, iron and vanadium doped titanium dioxide. React Kinet Mech Catal 111(1):393–414

34. Cui Y, Chen W-F, Bastide A, Zhang X, Koshy P, Sorrell CC (2019) Effect of precursor dopant valence state on the photocatalytic performance of Mo^{3+}-or Mo^{5+}-doped TiO_2 thin films. J Phys Chem Solids 126:314–321

35. Jiang Y, Chen W-F, Koshy P, Sorrell CC (2019) Enhanced photocatalytic performance of nanostructured TiO_2 thin films through combined effects of polymer conjugation and Mo-doping. J Mater Sci 54(7):5266–5279

36. Chen W-F, Chen H, Koshy P, Nakaruk A, Sorrell CC (2018) Effect of doping on the properties and photocatalytic performance of titania thin films on glass substrates: single-ion doping with cobalt or molybdenum. Mater Chem Phys 205:334–346

37. Wang Z, Chen C, Wu F, Zou B, Zhao M, Wang J, Feng C (2009) Photodegradation of rhodamine B under visible light by bimetal codoped TiO_2 nanocrystals. J Hazard Mater 164(2–3):615–620

38. Lin MZ, Chen H, Chen W-F, Nakaruk A, Koshy P, Sorrell CC (2014) Effect of single-cation doping and codoping with Mn and Fe on the photocatalytic performance of TiO_2 thin films. Int J Hydrogen Energy 39(36):21500–21511

39. Chen W-F, Koshy P, Sorrell CC (2015) Effect of intervalence charge transfer on photocatalytic performance of cobalt-and

vanadium-codoped TiO_2 thin films. Int J Hydrogen Energy 40(46):16215–16229

40. Emmett JL, Douthit TR (1993) Heat treating the sapphires of rock creek. Gems Gemol 29(4):250–272

41. Ren H, Koshy P, Cao F, Sorrell CC (2016) Multivalence charge transfer in doped and codoped photocatalytic TiO_2. Inorg Chem 55(16):8071–8081

42. Chen H-K, Chen W-F, Koshy P, Adabifiroozjaei E, Liu R, Sheppard LR, Sorrell CC (2016) Effect of tungsten-doping on the properties and photocatalytic performance of titania thin films on glass substrates. J Taiwan Inst Chem Eng 67:202–210

43. Chen W-F, Koshy P, Adler L, Sorrell CC (2017) Photocatalytic activity of V-doped TiO_2 thin films for the degradation of methylene blue and rhodamine B dye solutions. J Aust Ceram Soc 53(2):569–576

44. Chung L, Chen W-F, Koshy P, Sorrell CC (2017) Effect of Ce-doping on the photocatalytic performance of TiO_2 thin films. Mater Chem Phys 197:236–239

45. Hanaor DA, Sorrell CC (2014) Sand supported mixed-phase TiO_2 photocatalysts for water decontamination applications. Adv Eng Mater 16(2):248–254

46. Kabir II, Sheppard LR, Liu R, Yao Y, Zhu Q, Chen W-F, Koshy P, Sorrell CC (2018) Contamination of TiO_2 thin films spin coated on rutile and fused silica substrates. Surf Coat Technol 354:369–382

47. Tauc J, Menth A (1972) State in the gap. J Non-Cryst Solids 8–10:569–585

48. Shirkhanzadeh M (1995) XRD and XPS characterization of superplastic TiO_2 coatings prepared on Ti_6Al_4V surgical alloy by an electrochemical method. J Mater Sci Mater Med 6(4):206–210

49. Nakamura I, Negishi N, Kutsuna S, Ihara T, Sugihara S, Takeuchi K (2000) Role of oxygen vacancy in the plasma-treated TiO_2 photocatalyst with visible light activity for NO removal. J Mol Catal A Chem 161(1–2):205–212

50. Naumkin AV, Kraut-Vass A, Gaarenstroom SW, Powell CJ (2012) NIST X-ray Photoelectron Spectroscopy Database, NIST Standard Reference Database 20, Version 4.1. US Department of Commerce, Washington

51. Bevy LP (2005) New developments in catalysis research. Nova Publishers, New York

52. Marquis FS (2017) Proceedings of the 8th Pacific Rim international conference on advanced materials and processing (PRICM-8). Springer

53. Allen LC (1989) Electronegativity is the average one-electron energy of the valence–shell electrons in ground-state free atoms. J Am Chem Soc 111(25):9003–9014

54. Allred AL, Rochow EG (1958) A scale of electronegativity based on electrostatic force. Inorg Nucl Chem 5(4):264–268

55. Little EJ Jr., Jones MM (1960) A complete table of electronegativities. J Chem Educ 37(5):231–233

56. Putz MV, Russo N, Sicilia E (2005) About the Mulliken electronegativity in DFT. Theor Chem Acc 114(1–3):38–45

57. Pauling L (1932) The nature of the chemical bond. IV. The energy of single bonds and the relative electronegativity of atoms. J Am Chem Soc 54(9):3570–3582

58. Pearson RG (1988) Absolute electronegativity and hardness: application to inorganic chemistry. Inorg Chem 27(4):734–740

59. Sanderson RT (1983) Electronegativity and bond energy. J Am Chem Soc 105(8):2259–2261

60. Shannon RD (1976) Revised effective ionic radii and systematic studies of interatomic distances in halides and chalcogenides. Acta Cryst A 32:751–767

61. Kroger FA, Vink HJ (1958) Relations between the concentrations of imperfections in crystalline solids. J Phys Chem Solids 5:307–435

62. Linsebigler AL, Lu G, Yates JT Jr. (1995) Photocatalysis on TiO_2 surfaces: principles, mechanisms, and selected results. Chem Rev 95(3):735–758